ACOUSTIC MICROSCOPY

Acoustic microscopy involves imaging the elastic properties of surface or subsurface regions using acoustic waves, as well as measuring the mechanical properties on a microscopic scale. In most of the work done so far, this has involved focusing acoustic waves by an acoustic lens which is mechanically scanned over the field of view. Following the initial work of Sokolov (1), the real start of the field was the development of the scanning acoustic microscope (SAM) by Lemons and Quate in 1973 (2,3). This was essentially an extension of the traditional focused C scan ultrasonic imaging system, which is a broadband scanned ultrasonic imaging system using a spherical lens of high *f* number to image defects in the interior of opaque samples.

The heart of the Lemons–Quate SAM is the acoustic lens, shown in Fig. 1 (4). A radiofrequency (RF) tone burst, typically 50 ns to 500 ns wide and containing a single RF frequency in the range 10 MHz to 1000 MHz is applied to a piezoelectric transducer fixed on the top surface of the acoustic lens body. The transducer converts the RF pulse into an ultrasonic wave with the same frequency that is emitted into the lens body. This ultrasonic wave propagates to the opposite face and impinges on the surface of a spherical cavity that has been carefully ground and polished in the lens body. The lens cavity is coupled by a liquid drop, usually water, to the sample surface, which is placed at the focal point of the spherical lens. The ultrasonic pulse is thus transmitted into the water, comes to a focus, and then is reflected back to trace out the same path in reverse. The amplitude of the reflected pulse is proportional to the difference between the acoustic properties of the sample and those of water at the focal point, so that the amplitude gives a measure of the microscopic

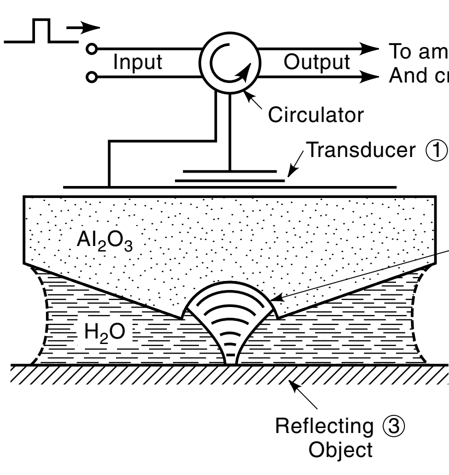

Figure 1. The geometry of the acoustic lens for the reflection mode of the SAM. (From Ref. 4 with permission.)

properties of the sample at that point. The pulse is then reconverted to an RF pulse by the inverse piezoelectric effect, and this RF pulse is then fed into an RF receiver tuned to the appropriate frequency. The average amplitude of the pulse is determined, converted into a digital signal, and sent to a computer imaging system. The lens is then mechanically displaced a small distance and the whole process is repeated. In order to form an image, the lens is scanned successively from point to point along a line, which typically contains 500 points or pixels. Successive lines are then scanned in raster fashion, so that an image is formed in the same way as on a TV screen. A very detailed account of the SAM is given by Briggs (5), and where possible the notation used there will be followed in this article.

Despite its simplicity, the spherical acoustic lens is an almost perfect imaging device. All of the usual aberrations that complicate enormously the design of optical microscopes are absent from the SAM, principally because the imaging is always done on axis at a single frequency. An essential aspect is that the acoustic velocity of the lens is chosen to be very much greater than that of the coupling liquid, which reduces spherical aberration to a minimum. The result is that the spatial resolution, the smallest distance between neighboring image points, is close to its ideal theoretical value, being limited by diffraction, or the natural broadening of any wave focused to a point. As Lord Rayleigh showed, a point can best be described as a circle of diameter equal to the wavelength of the wave that is used for imaging. The wavelength is inversely proportional to the frequency, so to increase the resolution, hence decrease the size of the smallest circle, the frequency must be increased, and herein lies one of the main design considerations of acoustic lenses.

With increase in frequency, while the resolution increases proportionally, the acoustic losses increase even faster, so that eventually the reflected pulse becomes too small to measure. Hence systematic steps must be taken to reduce losses if the goal is to maximize the resolution. From the RF source to the receiver, such steps include the following: maximize peak power and minimize pulse width to separate closely spaced echoes, match electrical impedance between transducer and the electronics to maximize power transfer, use the most efficient and low-loss transducer possible, choose lens body material to be low loss and high velocity, use a highly oriented single crystal to avoid beam steering and ensure that maximum acoustic intensity reaches the cavity, use a small diameter lens to reduce transmission length in the liquid, use acoustic matching layers to maximize transmission into the liquid and reduce stray reflected echoes in the lens body, choose a low attenuation liquid, and use a high-sensitivity, low-noise receiver. These conditions are easy to fulfill at 10 MHz or 100 MHz; at 2 GHz, the upper operating frequency of the Leitz ELSAM, where the resolution is about that of the standard optical microscope, they are exceedingly difficult, and indeed relatively little work has been done in this range.

Reflection SAM is generally done in one of two imaging modes: (1) high resolution surface imaging, where a high-frequency, high numerical aperture (NA) lens is chosen or (2) subsurface imaging, for which a sufficiently low-frequency and low NA lens is used, so that most of the ultrasonic wave penetrates into the sample. Many examples of reflection SAM imaging can be given, including biomedical imaging of soft and hard tissues, thin films, substrate materials, subsurface

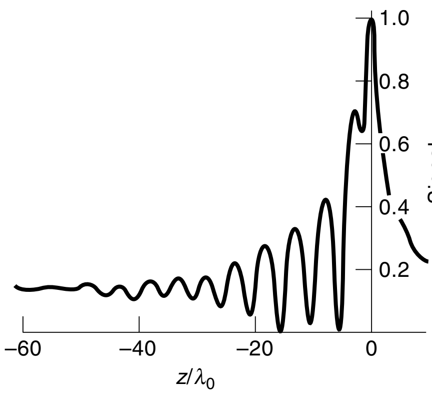

Figure 2. $V(z)$ curve for fused quartz and water at 225 MHz. (From Ref. 5 with permission of Oxford University Press.)

defects in materials and devices, stress, cracks, etc. An example of each type will be given in the next section. With increasing frequency, the most common applications are: (1) Low frequency regime (10 MHz to 100 MHz) is generally used for detecting defects in microelectronic chips and other subsurface damage. (2) The medium-frequency range (100 MHz to 1000 MHz) is generally used for a wide variety of nondestructive evaluation (NDE) and biological samples, as well as quantitative microscopy (to be described). (3) High-frequency range above 1 GHz is restricted to special studies needing very high resolution. The highest resolution attained in this range is 20 nm using liquid helium as a coupling liquid.

In the early days of acoustic microscopy it was discovered that slight defocusing is needed to obtain high-contrast images. A theoretical understanding of this phenomenon quickly leads to the realization that one could obtain quantitative information from the SAM by continuously defocusing and bringing the sample toward the lens for a fixed x, y position of the lens axis (z direction). Periodic variations of the voltage of the reflected signal are observed, the so-called $V(z)$ phenomenon (6). Typical behavior is seen in Fig. 2, which shows a series of oscillations of $V(z)$, with constant distance Δz between the minima. It is possible to obtain the Rayleigh surface wave velocity directly from Δz and this forms the basis for the quantitative applications of the SAM.

A simple explanation for the $V(z)$ effect is as follows: One can divide the acoustic wave incident on the sample into two beams, a central one (C) and an outside cone of rays (R), as shown in Fig. 3. The central beam is directly reflected by the sample and serves as a reference. The outer conical beam arrives at the sample surface at the appropriate angle to set up Rayleigh surface waves. These are reradiated or leaked back into the liquid and eventually return to the transducer. These two components interfere constructively or destructively, depending on the lens-to-sample distance, which results in the set of interference fringes observed in $V(z)$.

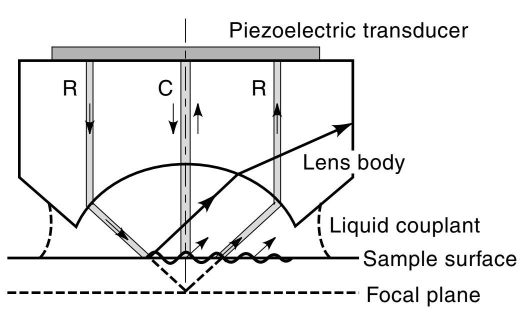

Figure 3. Simplified two-beam model to show the physical origin of $V(z)$.

The consequences of the $V(z)$ effect are many, and in fact the phenomenon is fundamentally important for all aspects of acoustic microscopy. For the spherical lens, the Rayleigh surface waves are excited in all directions and some appropriate average pertains for each point on the surface. This is important for high-contrast imaging, for example, of the grain structure of an alloy. Each grain has a particular crystallographic orientation compared to its neighbor, and so each one has a different average surface wave velocity. This leads to a different reflected signal for each grain via the $V(z)$ effect, so that some grains will give a maximum reflection and others a minimum one. The situation will be reversed for some other neighboring value of z. All of this results in the SAM having very high intrinsic contrast, so that special staining or etching techniques often used in metallography are not required. This identifies one important advantage of SAM for studying metals, alloys, and inhomogeneous samples.

One specific application of quantitative acoustic microscopy has been the development of the line focus beam (LFB) for directional measurements (7). The spherical Lemons-Quate lens is replaced by a cylindrical lens, so that the focal point is replaced by a focal line. Of course it is no longer possible to obtain acoustic images, but there are compensations for quantitative microscopy. The $V(z)$ phenomenon remains essentially the same, with the important proviso that Rayleigh surface waves are now emitted in the direction perpendicular to the focal line, and so the $V(z)$ can be related to a specific propagation on the sample surface. By rotating the lens one can measure the anisotropy in the Rayleigh wave velocity and, by an inversion procedure, the elastic constants. These effects have been studied by many workers. It has been shown that accuracies of the order of 10^{-4} in the velocities are possible, providing that displacements, water temperature, and frequency are measured very accurately. Examples of studies carried out with the LFB are crystal anisotropy, anisotropic films on substrates, wafer mapping, optical fibers, etc.

Another different but complementary tool to the SAM is the scanning laser acoustic microscope (SLAM) (8). As seen in Fig. 4, in the SLAM the sample is irradiated from the back side by a continuous uniform beam of ultrasound, which is then transmitted to the front surface. The impinging ultrasonic beam creates a surface disturbance, which is imaged by a scanning laser beam in real time (30 frames per second). Since the transmitted ultrasound intensity is affected by defects in the bulk of the sample, these can be detected by SLAM imaging. The technique has been widely used for evaluating bonding, delamination, defects in microelectronic devices, biomedical imaging, and many other applications. The real-time aspect is particularly interesting for NDE, for example to study the propagation of a crack in a material under stress. Other advantages include the possibility of detecting surface waves of extremely small amplitudes ($\sim 10^{-6}$ nm/ $\sqrt{\text{Hz}}$ bandwidth) and doing plane by plane imaging by a holographic technique. The resolution of the acoustic images is limited by the ultrasound wavelength, about 50 μm at 100 MHz.

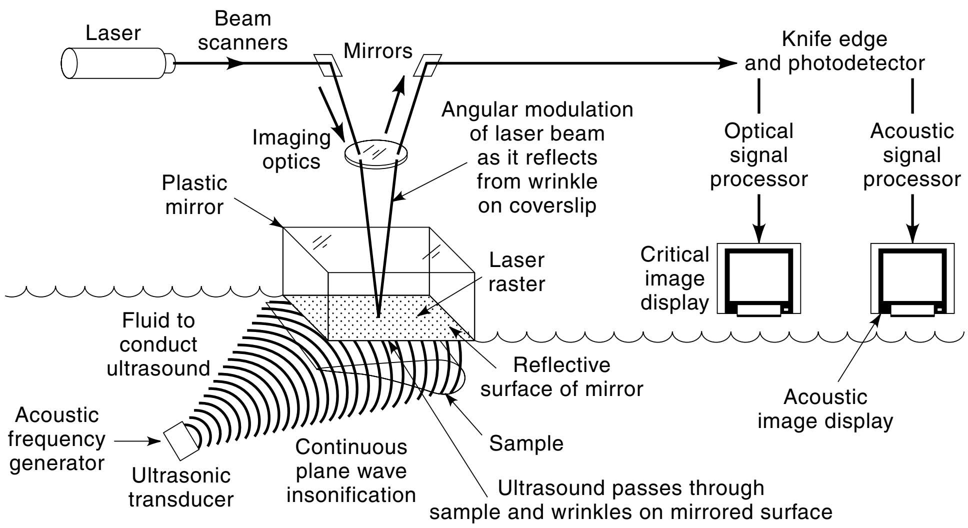

Figure 4. Block diagram of the scanning laser acoustic microscope. (From SONOSCAN prospectus, with permission.)

CONVENTIONAL ACOUSTIC MICROSCOPY

Resolution

By the very fact of on-axis imaging at a single frequency, four out of five aberrations identified in optical microscopy are immediately eliminated; chromatic, barrel and pincushion distortion, and astigmatism. That remaining, spherical aberration, can easily be eliminated, both in theory and in practice, in the following way. Using geometrical optics, in first-order theory, the paraxial focal length q measured from the lens surface is given by

$$q = r_0/(1-n) \tag{1}$$

where r_0 is the lens radius and $n = n_1/n_2$ where n_1 is the refractive index of the lens and n_2 that of the coupling liquid. In the SAM $n = v_0/v_\ell$ where v_0 is the sound velocity in the coupling fluid and v_ℓ the longitudinal wave velocity in the lens body. Hence $n \ll 1$ and the focal point is approximately at the center of curvature. The effect of spherical aberration (SA) can be calculated in third-order theory. Rays incident at the full lens aperture (a distance h from the lens axis) focus at a distance s_2 from lens surface and it is easily shown that (5):

$$\frac{1}{s_2} = \frac{1}{q} + \frac{n^2h^2}{2qr_0^2} \tag{2}$$

The aberration corresponds to the second term, which can be made sufficiently small with a small enough value of n. An alternative approach is to describe SA as a small deviation W from a spherical wave front (3):

$$W(\theta, n) \cong 2r_0n^2(1-n)\left[\sin^4\left(\frac{\theta}{2}\right) + 2n(1-n)\sin^6\left(\frac{\theta}{2}\right)\right] \tag{3}$$

where θ is the lens aperture. This result also shows that the SA scales with the size of the lens and is thus reduced even further in the small lenses used at high frequencies. Finally, it has been shown by Lemons and Quate (3) that slight defocusing toward the lens can be used to reduce SA.

The result is that the resolution is diffraction limited. According to the Rayleigh criterion, the spatial resolution limited by diffraction is given by:

$$w = 0.61\lambda_0/\text{NA} \tag{4}$$

where NA = aperture radius divided by the focal length. The numerical coefficient can be improved by signal processing, but the essential result is that the spatial resolution is limited by the wavelength. For surface imaging, where maximum resolution is normally desirable, the NA is normally made as large as possible. As described before, increasing the resolution can be most directly accomplished by raising the frequency, and the acoustic attenuation in the liquid then becomes the main parameter. A resolution coefficient has been defined to compare the best resolution that can be obtained for various coupling liquids (9), taking into account the focal length and the attenuation in the liquid. This resolution coefficient R_c is defined as

$$R_c = \sqrt{v_0^3\alpha_0} \tag{5}$$

where $\alpha = \alpha_0 f^2$ for a given liquid. Representative values of the liquid parameters and R_c are given in Table 1. In general, one has to go to cryogenic liquids to obtain significant improvement over water. Relevant acoustic parameters for solids, including those used for lens fabrication, are given in Table 2.

Various strategies can be employed to decrease w, depending on the experimental conditions. The following points can be made:

1. For the vast majority of applications at not too high frequencies, water is the simplest and almost optimal choice
2. The liquid metals gallium and mercury have attractive acoustic properties (9), but they are difficult to work with, and this fact has greatly reduced their use in practical applications
3. Significant gains can be achieved by heating the water to 60°C or higher (2)

Table 1. Acoustic Parameters of Various Fluids

Fluid	Temperature T(K)	Velocity, ν_0 (μm ns^{-1})	Impedance, Z (Mrayl)	Attenuation, α_0 (dB μm^{-1}GHz^{-2})	Resolution Coefficient, R_c (μm dB$^{1/2}$ ns$^{-1/2}$)
Water	298	1.495	1.49	0.191	0.799
Water	333	1.551	1.525	0.086	0.566
Methanol	303	1.088	0.866	0.262	0.581
Ethanol	303	1.127	0.890	0.421	0.776
Acetone	303	1.158	0.916	0.469	0.853
Carbon tetrachloride	298	0.930	1.482	4.67	1.94
Hydrogen peroxide	298	1.545	2.26	0.087	0.566
Carbon disulfide	298	1,310	1.65	0.087*	0.442
Mercury	297	1.449	19.7	0.050	0.391
Gallium	303	2.87	17.5	0.0137	0.570
Air (dry)	273	0.33145	0.4286×10^{-3}	—	—
Air (dry)	293	0.34337	0.4137×10^{-3}	1.6×10^5	80
Air (dry)	373	0.386	—	—	—
Argon	293	0.323	0.023	3.58	0.347
Argon	293	0.323	0.145	0.721	0.156
Xenon	293	0.178	0.042	8.28	0.216
Oxygen	90	0.900	1.0	0.086	0.250
Nitrogen	77	0.850	0.68	0.120	0.271
Hydrogen	20	1.19	0.08	0.049	0.287
Xenon	166	0.63	1.8	0.191	0.219
Argon	87	0.84	1.2	0.132	0.280
Neon	27	0.60	0.72	0.201	0.208
Helium	4.2	0.183	0.023	1.966	0.110
Helium	1.95	0.227	0.033	0.610	0.084
Helium	0.4	0.238	0.035	0.015*	0.014
Helium	0.1	0.238	0.0345	4×10^{-5}*	7×10^{-4}

* For these two fluids the attenuations do not follow a simple f^2 law, and the values given correspond to measurements at 3 GHz for carbon disulfide and at 1 GHz for helium at 0.4 K and at 0.1 K.
From Ref. 5 with permission of Oxford University Press.

Table 2. Acoustic Parameters of Various Solids

Material	Axis	Density ρ ($\times 10^3$ kg/m^3)	Velocity C ($\times 10^3$ m/s)	Impedance Z ($\times 10^6$ kg/m^2 s)	Absorption x/v^2 ($\times 10^{-15}$ s^2/m)	Structure
Sapphire	Z	3.986	11.1	44.3	0.0021	trig $\bar{3}$ m
YAG	[001]	4.55	8.43	38.34	0.0034	cubic m3m
Rutile	Z	4.26	7.90	33.6	—	tetr 4 mmm
Lithium niobate	Z	4.70	7.33	34.0	0.0047	trig 3m
Fused quartz	—	2.20	5.97	13.1	0.13	isotropic
Glass (light borate crown)	—	2.243	5.09	11.42	—	isotropic
Aluminum	—	2.695	6.35	17.2	0.86	polycrystalline
Gold	—	19.30	3.21	61.3	2.3	polycrystalline
Silver	—	10.49	3.44	36.1	—	polycrystalline
Lucite	—	1.182	2.68	3.16	—	isotropic
Polyethylene	—	0.900	1.94	1.75	—	isotropic
Polystyrene	—	1.056	2.34	2.47	—	isotropic
Mylar	—	1.18	2.54	3.0	92	isotropic

From Ref. 3 with permission.

4. High-pressure gases such as argon are in principle attractive; however, the acoustic impedance difference between sample and gas means that topography dominates the image properties
5. Cryogenic liquids can be used to advantage because of their low attenuation and velocity (10); however, the acoustic impedance mismatch is so great that the reflectivity is almost 100% everywhere on the sample surface, so that topography again dominates; also, this is not a practical route for most industrial applications.
6. Nonlinear enhancement of the resolution can be used to advantage. The high acoustic intensities at the focus mean that harmonic generation is very pronounced in this region. Rugar (11) showed that the threshold power for significant generation of the second harmonic is given by

$$P_0 = \frac{4s_d L(\mathrm{NA})^2}{f^2} \tag{6}$$

where

$$L = \frac{\rho_0 v_0^5}{16\pi^3 \beta_L^2} \tag{7}$$

where β_L is the fluid nonlinear coupling constant.

It is known that an increase in resolution by $\sqrt{2}$ is obtained by generation of the second harmonic at the focus, and Ruger (11) showed that in reflection microscopy this enhancement is maintained even though the second harmonic is subsequently down-converted to the fundamental. This work was extended by Germain and Cheeke (12), who showed experimentally that a similar resolution enhancement by $\sqrt{n}$ occurred for higher harmonics n and that significant resolution improvement could be obtained by detecting them directly at the focal plane in a transmission configuration. They showed that this mode of operation is particularly advantageous for samples in solution and biological samples.

Lens Design

The present discussion is for the most common case, that of surface imaging or quantitative microscopy. As already stated, the basic design parameter is the operating frequency, which, together with the choice of coupling fluid, determines the resolution. These two parameters in turn lead to the maximum travel path in the liquid, hence the lens cavity radius r_0. This will be set by specifying the maximum liquid attenuation losses, which might be typically of the order of 50 dB, for a travel path equal to twice the focal length q. For water coupling, typical values of r_0 are 5 mm at 10 MHz and 50 μm at 1 GHz. The lens material is chosen to keep $n \ll 1$ to avoid spherical aberration and also to keep attenuation in the lens body to be as small as possible.

The lens cavity radius is an important parameter for several reasons: (1) it determines the maximum pulse width, as the reflection from the front face of the lens and from the sample at the focal plane must be clearly time resolved; (2) this pulse width determines the maximum receiver bandwidth and hence the receiver noise figure; (3) the pulse width also determines the axial resolution or depth of field for the case of subsurface imaging. Apart from resolution considerations, the choice of the NA follows directly from the lens diameter. For surface imaging, it is critical that the NA be sufficiently large to include the specimen Rayleigh angle, which is an essential element of the contrast mechanism.

Obtaining a high signal-to-noise ratio is important for image quality, and one way to improve this is to maximize the acoustic intensity reaching the lens. Some important steps are: (1) matching the transducer electrically to 50 Ω to both source and receiver; (2) using high-performance transducers such as bonded lithium niobate or PZT up to 200 MHz or RF-sputtered zinc oxide (ZnO) or aluminum nitride (AlN) above that frequency; (3) minimizing acoustic loss in the lens body due to diffraction by placing the lens cavity at the Fresnel distance z_0 from the transducer: $z_0 = a^2/\lambda$ where a is the transducer radius. For example, at $f = 2$ GHz and $a = 60$ μm, $z_0 = 1$ mm. The required condition is not easy to achieve at low frequencies as z_0 can become quite large, which would lead to impracticably long lens bodies. However signal-to-noise is not usually a problem at low frequencies. The effect of changing the transducer-to-lens distance on the lens illumination and on the point-spread function has been studied in detail by Chou et al. (13); (4) using matching layers on the lens surface to maximize the transmission in both directions, which becomes essential at sufficiently high frequencies. Because of the awkward range of thickness required at low frequencies, impedance matching is difficult to do below 100 MHz, but again it is not really necessary. The matching layer should be a quarter wavelength thick with an acoustic impedance $Z = \sqrt{Z_1 Z_2}$ where Z_1 and Z_2 are the acoustic impedances of the lens body and coupling fluid, respectively. Sputtered glass or similar materials are usually used. The quarter-wavelength matching layer also acts as an antireflection coating and as such reduces unwanted reflections inside the lens body. This gives a direct improvement to the signal-to-noise ratio as it facilitates time resolution of the small focal point echo from spurious signals. For order-of-magnitude considerations at 1 GHz, if we assume a receiver dynamic range of the order of 120 dB, then this might be divided as follows: 30 dB for various losses in the lens, 60 dB in the liquid, and 30 dB for providing sufficient image contrast. These considerations are further developed by Briggs (5).

Contrast Mechanisms and Quantitative Measurements

$V(z)$ Theory. A typical $V(z)$ curve is shown in Fig. 2; by convention, negative z corresponds to a decreased lens-to-sample distance. The two main interfering beams are shown in Fig. 3, and those that appear to come from the focal point interfere at the piezoelectric transducer, which is sensitive to the phase. By simple geometry from Fig. 3, the relative phase difference between the two beams is

$$\phi_G - \phi_R = -2kz(1 - \cos\theta_R) + \pi \tag{8}$$

where θ_R is the Rayleigh angle, defined as sin $\theta_R = V_0/V_R$. Clearly the interference condition depends on z, giving rise to the series of minima seen in Fig. 2. The period of the oscillations is

$$\Delta z = \frac{2\pi}{2k(1 - \cos\theta_R)} \tag{9}$$

so that measurement of z for a given f and v_o gives θ_R, hence v_R, for the sample at this position. Similar considerations give for the attenuation

$$\Delta\alpha = 2z(\alpha_0 \sec\theta_R - \alpha_R \tan\theta_R) \tag{10}$$

However, the attenuation is much more difficult to obtain accurately, and most of the work has been done on measurement of v_R.

While the simple two-beam model is useful for understanding the physics of $V(z)$, many simplifications have been made. A more rigorous mathematical treatment of the phenomenon is provided by scalar wave theory (14), which is used to describe the refraction of all acoustic waves over the lens aperture into the liquid. For a given z the result is

$$V(z) = \int_0^{\pi/2} P(\theta)R(\theta)e^{-i2zk\cos\theta} \sin\theta\cos\theta\, d\theta \tag{11}$$

where $P(\theta)$ is the pupil function that characterizes the lens transmission properties, which depend on the geometry and the lens material parameters and $R(\theta)$ is the amplitude reflectance function. By redefining variables such that $u = kz$, $t = 1/\pi \cos\theta$, and $Q(t) = P(t)\,R(t)t$, we find

$$V(u) = \int_0^{1/\pi} Q(t)e^{-i2\pi ut}\, dt \tag{12}$$

so that $V(u)$ and $Q(t)$ are a Fourier transform pair for a lens with a known pupil function. Thus the measurement of the full $V(z)$ curve over the full range of z should lead in principle to a determination of $R(\theta)$, which will be given below. Analogous treatment can be given for transmission (15), although the applications have been much less numerous. The formulation is:

$$A(z) = \int_0^{\pi/2} P(\theta)T(\theta)e^{-i(z-d)k\cos\theta} \sin\theta\cos\theta\, d\theta \tag{13}$$

where $P(\theta)$ is the lens function for the two lenses and $T(\theta)$ is the transmission function for a layer of thickness d for incident and refracted angles θ.

In addition to the wave theory, a ray model more complete than the simplified version already mentioned has also been developed (16). It is an interesting complement to the wave theory, as various modes such as surface skimming bulk waves may be put explicitly into the model, as described in detail in (5).

Reflectance Function from Fourier Inversion. Inversion of the wave theory gives:

$$R_t(t) = \frac{1}{P_t(t)t} \int_{-\infty}^{\infty} \frac{V(u)}{V_0} e^{i2\pi ut}\, du \tag{14}$$

so that measurement of $V(u)$ can give $R(\theta)$. As mentioned by Briggs (5), there are several precautions to be observed with this formula: (1) one can only obtain $R(\theta)$ for the range of angles included within the lens opening, (2) the full curve $V(u)$ is needed, as truncation can cause errors, (3) the results are sensitive to attenuation associated with fluid loading, especially at high frequencies, and (4) $V(u)$ is a complex function, so measurement of the amplitude and phase are needed. The first measurements were carried out by Liang et al. (17) seen in Fig. 5 for water-fused silica interfaces at 10 MHz. A lead sample, for which no Rayleigh waves are excited in this case, was used as a reference to obtain the pupil function. The most spectacular result was observation of an expected phase change of 2π at the Rayleigh angle, which allowed accurate determination of v_R. A dip in the amplitude is also seen at θ_R; this is usually due to damping of the Rayleigh wave, but care must be taken as such dips could also be due to anisotropy and/or truncation of the data.

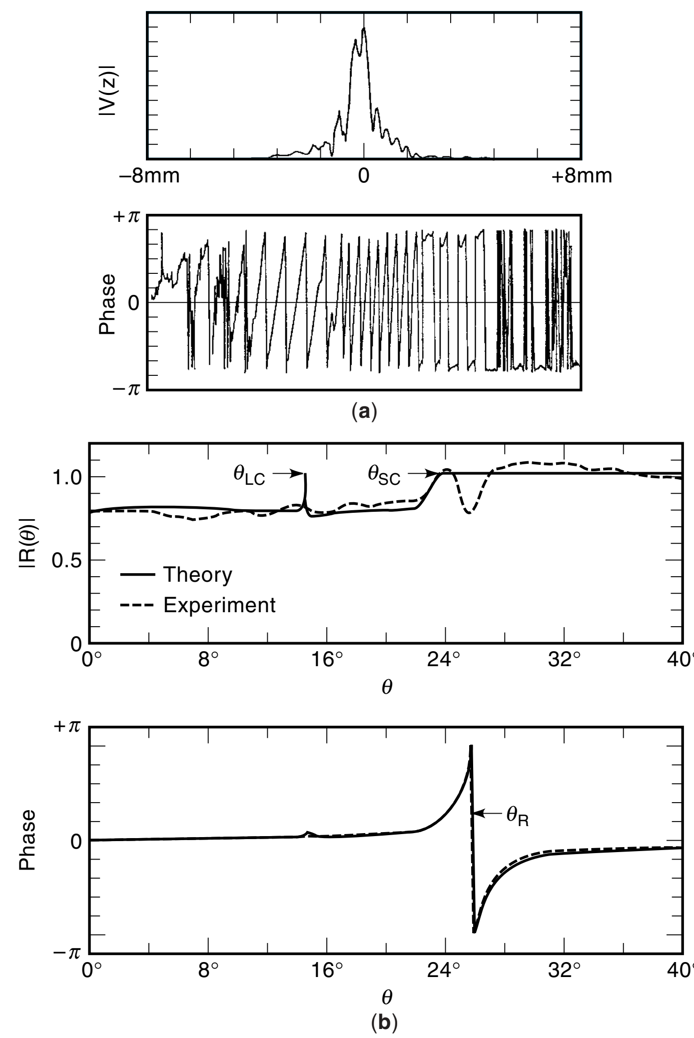

Figure 5. (a) Experimental $V(z)$ of water-fused silica interface at 10.17 MHz. (b) Comparison of the theoretical and experimental reflectance function for a water-fused silica interface. (From Ref. 17 with permission.)

Line Focus Beam. Developed by Kushibiki and co-workers, (7) the line focus beam (LFB) technique exploits Rayleigh waves emitted perpendicular to the focal line of a cylindrical lens. The generally accepted analysis uses a ray approach that can be summarized as follows. The reflected signal can be written as

$$V = V_G + V_R \tag{15}$$

where V_R is the Rayleigh wave contribution and V_G is due to the sum of all other scattered waves.

For square law detection

$$|V|^2 = |V_G|^2 + |V_R|^2 + 2|V_G||V_R|\cos\theta \tag{16}$$

where θ is the phase angle between V_G and V_R and all terms are z dependent. The measuring system is calibrated using a lead sample; to a good approximation, $V_L = V_G$. Two assumptions are then made to complete the analysis for the LFB:

1. $|V_R| \ll |V_G|$, which reduces to:

$$|V| - |V_L| = |V_R|\cos\phi \tag{17}$$

2. The phase depends linearly on z, leading to

$$\phi = -2kz(1-\cos\theta_R) + \pi \tag{18}$$

Neglecting attenuation, it is found that the spatial frequency of the Fourier transform of $V(z)$ is centered at

$$\xi_0 = \frac{2\pi}{\Delta z} = 2k(1-\cos\theta_R) \tag{19}$$

Taking attenuation into account, the final results are expressed as:

$$v_R = v_0\left\{1-\left(1-\frac{v_0\xi_0}{4\pi f}\right)^2\right\}^{-1/2} \tag{20}$$

$$\alpha_N = \frac{\alpha\cos\theta_R + 2\alpha_0}{2k_R\sin\theta_R} \tag{21}$$

Several experimental precautions are needed to obtain very high accuracy for v_R and α_N with the LFB; steps include use of goniometers for tilt alignment, careful temperature control of the water drop, and careful measurement of the lead reference calibration curve. Likewise, there are several steps in the data analysis necessary to get accurate data reduction for Fourier analysis, including filtering and subtracting out V_L by an iterative procedure. Full details are given in Ref. 7. The accuracy of the LFB can be written in terms of precision in temperature, distance, and frequency measurements as:

$$\frac{\delta v_\mathrm{R}}{v_\mathrm{R}} = \sqrt{\left\{(0.0011\delta T)^2 + \left(0.464\frac{\delta f}{f}\right)^2 + \left(0.464\frac{\delta\Delta z}{\Delta z}\right)^2\right\}} \tag{22}$$

from which it can be deduced that for a relative accuracy of 10^{-3} in $\Delta v/v$, ΔT is needed to ± 0.9°C, $\Delta f/f$ to 0.2% and $\Delta z/z$ to 0.2%, while for a relative accuracy of 10^{-4}, ten times greater precision is needed for each parameter. Full details are given in Ref. 7 for determinations of $\Delta v/v$ and α_N for over 30 different materials. Accuracies of 10^{-4} for $\Delta v/v$ and 2% for α_N are claimed.

A simplified form of the LFB has been developed by Hsu et al. (18). Basically this device uses a 10 MHz lenseless line focus transducer to determine velocities of various surface modes by $V(t, z)$ scans over large areas of the sample surface, and this as a function of propagation direction. A significant disadvantage is the poor spatial resolution which for many applications may be compensated by the simplicity of the device. Another technique related to the LFB is the ultrasonic microspectrometer (UMSM). The device consists of a spherical lens source and a planar receiver mounted on a common goniometer (19). A broadband source is used and a fast Fourier transform (FFT) of the received signal gives the frequency variation. This device allows measurement of the reflectivity $R(\theta)$ with a spatial resolution of about 10 μm, with information also on the azimuthal angle variation. An early version was used for layer thickness determination by measuring the frequency at which Sezawa waves leak into the substrate. Subsequently the instrument was used for measurement of the velocity and attenuation of Rayleigh waves as a function of frequency and propagation direction.

Applications

Biological Samples. Ultrasound imaging and quantitative study of biological tissue have several characteristic differences from similar studies on materials. There is no flat, well-defined reflecting surface, and biological tissues are generally more homogeneous in their structures, typically with high attenuation and sound velocity in the range of that of water. Since the shear modulus is low and shear viscous damping is high, we are only concerned with longitudinal waves.

As a consequence, while the technology is generally the same as for materials, there are important differences. Transmission mode imaging or through transmission substrate reflection is much more frequently used, although the analog of reflection SAM, ultrasonic backscatter microscopy (UBM) has been used in some work. Traditionally, the frequency range for medical imagery has been below 10 MHz, although in some of the work to be described here this has been extended toward the 30 MHz to 100 MHz range. As in NDE, ceramic transducers with their high coupling coefficients are frequently employed, although polyvinylidene fluoride (PVDF) and copolymers find relatively more frequent use than in NDE because of their good impedance match to water. It should be noted that medical imaging has several imaging modes, namely A scan (amplitude/time trace as on the oscilloscope), B scan (section normal to the sample surface) and the usual C scan used for imaging materials.

Acoustic microscopy in the 10 MHz to 100 MHz range can be either in vivo or in vitro. Complete summaries and references to most available results are given in Refs. 20 and 21. One of the common imaging applications in this range is for dermatological diagnosis. A wide bandwidth and sufficiently high frequency of transducer and the electronics are essential to obtain sufficient axial and lateral resolution. Typically, the transducer is placed at the end of a lever and mechanically scanned by a dc motor, with acoustic coupling supplied by an ultrasonic gel. B scan is used to identify the various layers and interfaces of normal skin (epidermis, dermis, hypodermis) and muscle. One of the main applications is imaging of pathological skin in order to determine the size and depth of tumors, a complement to other techniques for determining malignancy. Inflammatory diseases such as psoriasis plaques can also be monitored by B scan. Most of the commercial units operate near 20 MHz. Recent work at 50 MHz shows that the depth of exploration is limited to about 4 mm at this frequency.

Another much studied area is that of opthalmological applications. At low frequencies (<15 MHz) commercial instruments are routinely used to measure dimensions of internal structures of the eye and to detect structures hidden by the eye lens. More recently, there have been developments of high-frequency (30 MHz to 100 MHz) biomicroscopes, which are useful for imaging small structures a few mm below the surface, for imaging the cornea for thickness and for state of corneal grafts, and for detecting cysts and tumors. This high-frequency work gives new, unique information on eye structures and is a promising area of development.

Intravascular ultrasaonic imaging is another important area in medical applications, where the main problem is detection of hardening of the arteries, or atherosclerosis. In vitro studies have been carried out to establish a correlation between ultrasonic images at about 50 MHz and histology. The agreement is excellent for detection of arterial wall thickening due to plaque in most arteries, and good calculation is also obtained for the more elastic carotid artery. In vivo ultrasonic imaging is under development, while in vivo ultrasound is already useful for diagnosis and monitoring during surgery. The prime advantages of acoustic imaging are good resolution and contrast and real-time imaging.

All of the very high-frequency (>500 MHz) work has been done by SAM. Developments have proceeded more slowly than originally anticipated, in part because of the difficulties in image interpretation, but also because it is not a well-known technique so that it has not been easy to make connections with traditional cell biology. Several studies have been made of cells in culture, notably fibroplasts. SAM can be used as a tool to measure (1) topography, with the aid of the observed interference fringes; (2) attenuation, which is, however, difficult to interpret because of model dependence and assumptions on homogeneity; and (3) reflectivity, which suffers from similar ambiguities. A key issue for image interpretation is the model used for the acoustic properties of the cytoplasm. An effective medium approach for the sound velocity in the saline/fibril system can be used, as for porous systems, for example. There are, at present, too many uncertainties in the acoustic parameters to provide a basis for interpretation of SAM images. Work is ongoing using all of the techniques of acoustic microscopy to elucidate the mechanical properties of cytoplasm.

Important work is under way to study cell dynamics by SAM. Interference reflectometry has been used to visualize the elasticity distribution in cells. A subtraction scheme (Sub-SAM) for images taken at different times has been used to image cell motility and relate this to changes in elasticity, topography, or attenuation. This is a promising tool in its ability to detect all motile responses to applied stimuli.

Films and Substrates. Achenbach and co-workers (22) have used the LFB to determine the elastic constants of isotropic materials in bulk, plate, or thin film configurations at a single frequency. The heart of the method is an inversion procedure in which best estimates of elastic constants are put into a theoretical model for $V(z)$ to calculate velocities and amplitudes of leaky waves, which are then compared with those determined experimentally by LFB. The difference, or deviation D, is used to adjust the input elastic constants, and the process is repeated until convergence by least squares is obtained. Good agreement, of the order of 1%, has been obtained for velocities for glass and aluminum in bulk form, glass plates, titanium films on gold, and a gold film on glass. The advantage of the method is that it only requires a single frequency measurement by LFB.

Anisotropic films on anisotropic substrates (22) have been studied as an extension of the inversion method for isotropic systems. The wave model is used as the starting point for calculating $V(z)$. The reflection coefficient is calculated for the anisotropic case by a matrix method, where layers are represented transfer matrices, which are multiplied together to give the reflection coefficient. The measured and calculated $V(z)$ give good overall agreement for various isotropic/anisotropic combinations, such as TiN films on MgO substrates. As in the previous section, the actual inversion procedure for determining elastic constants is carried out by comparing surface acoustic wave (SAW) velocities extracted from the experimental $V(z)$ curves with those calculated by finding the roots of the Christoffel equation. In making the comparison for anisotropic materials, the distinction must be made between regular SAW and pseudo-SAW; for the latter, v is greater than for out of plane transverse waves. These two components correspond to qualitatively different regions of the angular velocity variation for SAW.

For a given specimen, the most reliable inversion technique is to compare SAW velocities obtained experimentally and those calculated theoretically by an iteration process with minimization by a Simplex method over a wide range of frequencies. A less acceptable alternative is to measure a few frequencies or several specimens with different thicknesses at a single frequency, but the latter approach is based on the dubious assumption that the properties of films of different thicknesses remain the same.

Considerable work has been done on film thickness measurements by SAM. For medium thickness films (1 μm to 20 μm), UMSM has been demonstrated to be an effective real-time online device. This technique works for films such that the layer transverse wave velocity is smaller than that of the substrate. Dispersion calculations show that the two lowest frequency modes are the Rayleigh mode and the Sezawa mode, the latter having a low-frequency cut-off when it leaks into the substrate. It has been demonstrated in practical conditions in the UMSM that, when the frequency is scanned, a dip occurs at cut-off, which enables a determination of the film thickness (19). For very thin films ($d < 1$ μm), the thickness can be determined easily in the laboratory by a $V(z)$ measurement, given an appropriate knowledge of the film parameters.

Film adhesion is another important problem which, in principle, is ideally suitable for study by the SAM. There have been a number of studies, which have been well summarized in Ref. 23. The basic idea is to use a high NA acoustic lens, so as to excite Rayleigh and Lamb waves in the multilayer system. One can then compare experimentally measured dispersion curves to those predicted by the theory for various states of interfacial contact; perfect, intermediate or loss of contact. It was found that in the two limiting cases there was excellent agreement between theory and experiment, and that known imperfect interfaces fell between the two. Finally, it was found that surface skimming compressional waves were even more sensitive than generalized Lamb waves to the interface conditions.

NDE of Materials. Subsurface imaging is carried out by focusing an acoustic lens below the surface. Because of the acoustic mismatch between sample and coupling fluid, there is a need to maximize the acoustic energy transmitted into the sample. One way to do this is to choose a suitably low NA lens so as to avoid the generation of surface waves. Another is to use a coupling fluid that is as well acoustically matched as possible with the sample. A second consideration is to maximize the spatial resolution, which is degraded with respect to that at the surface because of the higher sound velocity in the sample. In addition, there are two focal points, as mode conversion at the interface creates both longitudinal and shear wave components. The acoustic pulse must be sufficiently short to allow temporal resolution of these two focal echoes. This can be facilitated by the use of pulse compression techniques, analogous to those used in commercial radar. Additional factors to take into account are the attenuation in the solid, which may be very high (composites) or very low (single crystals), and this will be a major factor in limiting the maximum imaging depth. The confocal nature of subsurface acoustic imaging is such that it is possible to obtain plane-by-plane image slices; a demonstration for composites is given in Ref. 24.

The presence of stress in materials can be measured by acoustic microscopy by the effect of stress on sound velocity via the third-order elastic constants. For surface and near surface stress, the SAM is a useful tool for detecting the presence of both applied and residual stress, with reasonably high spatial resolution depending on the approach that is used, by use of Rayleigh or surface skimming compressional waves (SSCW) detection. Applied stress leads to the acoustoelastic effect, the change in velocity due to an applied stress field. There is an advantage to using the LFB instead of more conventional SAW technology, because of the flexibility of liquid coupling and the directionality and the 1 or 2 mm spatial resolution provided. A demonstration of the technique has been given by Lee et al. (25) for 6061–T6 aluminum using Rayleigh waves and SSCW, and for polymethyl methacrylate (PMMA) using SSCW. Samples were cut in a dog bone shape and placed in a uniaxial loader, with strain gauges attached to the surface. Calibration was carried out using a uniform load and measuring velocity parallel and perpendicular to the loading direction as a function of strain and by measuring $v(\theta)$ for several fixed values of strain. This procedure gives the two principal acoustoelastic constants for the material, which allows subsequent measurements of unknown nonuniform stress fields. In both cases, good agreement was obtained with finite element calculations.

Near-surface residual stress can also be measured using the Rayleigh wave velocity. The study by Liang et al. (26) used time-resolved phase measurements of the Rayleigh waves using a spherical lens. Excellent agreement was obtained for the spatial variation of residual stress by comparison with actual Vickers hardness measurements. Again, the acoustic technique would require a calibration procedure for a given material.

It has also been shown that bulk stress in solids can be imaged using the acoustic microscope (27). The technique is based on measuring acoustic birefringence under applied stress. Shear modes created by mode conversion can be imaged; those propagating through the stressed region have a decreased amplitude compared to those that traverse stress-free regions. By comparing the two, one can measure and image the variation in a stress field throughout the volume of the sample. Longitudinal waves give complementary results, that is, maximum amplitude where the shear mode has minimum amplitude. Possible applications include residual stress detection and crack-induced stress in ceramics and composites.

Qualitative and quantitative assessment of crack forms, dimensions, and growth rates in materials is important for NDE, particularly in determining the estimated lifetime of industrial components. SAM imaging is well adapted to this problem, particularly because of its subsurface ability. One characteristic of SAM images of cracks is the strong fringing observed with spacing of $\lambda_R/2$, which clearly demonstrates that Rayleigh waves are involved. This conclusion is also confirmed by detailed theoretical analysis (5).

The smallest cracks that can be detected by SAM are determined by acoustic considerations for the minimum width (28). Since Rayleigh waves need to propagate in a continuous fashion and they involve a strong shear component, the viscous penetration depth determines the smallest crack width at a given frequency. This length varies as $\sqrt{1/f}$, and for water at 1 GHz it is about 18 nm. The minimum length is determined mainly by ultrasonic time of flight considerations as short pulse techniques are mainly used to determine this dimension. For example, a pulse width of about 8 ns is needed to detect a crack 100 μm long. The time of flight diffraction technique (TOFD) has been used to identify various possible paths from the acoustic lens to the crack and then by use of a ray model to identify the observed rebound echoes by transit time. The model was validated in plastic materials and then applied to the measurement of actual cracks in aluminum-lithium alloys down to a depth of 220 μm. The same technique was used to measure crack growth under elastic loading in aluminum alloys, and good agreement was obtained with subsequent destructive inspection. Crack detection is thoroughly explored in Ref. 29.

NDE of Devices. This section is concerned with two complementary areas of the application of acoustic microscopy to the NDE of microelectronic and optical devices. The first is the important industrial area of microelectronic packaging of single chips, stacked chips, multichip modules, and stacked modules. The need here is for low-cost, high-speed detection of packaging defects such as leaks, voids, delaminations, etc. and their visualization. The principles involved are based on those of subsurface imaging of defects and acoustic studies of defects as discussed above. Ideally, these tests will be carried out on-line in real time. The second is more laboratory level research and development to characterize the homogeneity of microelectronic chips and optical fibers, which is achieved by measuring the spatial variation of the acoustic parameters.

The application of SAM and SLAM to microelectronic packaging has been fully covered in Refs. 30 and 31, with many examples of acoustic and other images. In Ref. 31 the emphasis is put particularly on the complementary nature of SAM, SLAM, X rays, and optical and destructive analysis. One of the important areas is in the ceramic packaging of chips, where one of the chief issues is leaks in the lid sealing. Entry of moisture and other contaminants leads to corrosion or change in electrical properties. Fifty MHz SAM was shown to be a useful technique for lid seal inspection, giving depth-specific information and void detection for both solder and glass-seal devices. Shear-wave imaging was shown in Ref. 30 to give good resolution for void detection up to 2 mm depth. Failure in plastic-packaged devices was found to be due largely to differential contraction, and SAM was found to be useful for detecting internal cracking and delamination, and to be very complementary to X-ray inspection.

Die-attach, the bond between a semiconducting chip and the substrate, is another area where SAM and SLAM have proven very useful. Bond integrity is important to provide good thermal, electrical, and mechanical contact, which are all essential for proper device operation. Voids, cracking, and poor adhesion are among the main problems, and it is shown by numerous images in Refs. 30 and 31 that these can be detected by SAM and SLAM. SAM is good for work in the reflection mode and can give unique information on the disbond. Other special applications in microelectronic packaging include detection of voids at tape automated bonding (TAB) interfaces, poor adhesion at soldered joints and detection of delaminated leads. The detailed studies presented in Refs. 30 and 31 clearly show that SAM and SLAM are now indispensable diagnostic tools for microelectronic packaging.

Two other microscopic monitoring tools of device components and materials should be mentioned. Kushibiki et al. (32) have done extensive studies of wafer mapping using the LFB. For example, studies were carried out on a 36° *Y*-cut $LiTaO_3$ wafer to be used for shear horizontal (SH) SAW. Rayleigh-type SAW waves were excited along the *X* axis, as this direction was found to be most sensitive to chemical composition and elastic inhomogeneities. Experiments were carried out as a two-dimensional mapping of 6×6-mm squares over a 76 mm diameter wafer. The results showed that by measuring velocity variations it is possible to carry out physical and chemical quality control as follows: (1) V_{LSAW} was proportional to the Curie temperature varying as 0.52 m/s per °C, (2) variations of 0.03 Li_2O-mole % could be detected, (3) residual multidomains produced during poling were detected by elastic inhomogeneities. A similar study was carried out over the section of cladded optical fibers (33), where different sections were doped with GeO_2, F and B_2O_3 to produce a controlled variation in refractive index. The LFB was used to compare the profile of V_{LSAW} with that of the refractive index. Very good agreement was obtained indicating the potential of the LFB as a characterization tool for optical fibers and preforms.

PERSPECTIVES

Conventional acoustic microscopy is now a mature subject. Its use in the microelectronics industry as an NDE tool is becoming more frequent; there is still a need for faster, ideally real-time imaging in this area. The LFB technique is finding increasing application as a research tool. The high-frequency SAM is used mainly for specialized applications and its future may well be in the biological area. As for future development, it seems likely that this lies with the application of atomic force microscopy to acoustic imaging.

In conventional (far-field) acoustic microscopy, it is axiomatic that the spatial resolution is limited by the wavelength. However, this condition can be circumvented by using the principle of near-field imaging, in which a probe or pin hole is placed very close to the surface. If the size and distance *d* of the probe are very much less than the wavelength, then the resolution is limited by *d* and not λ. This principle is valid for any type of wave and was first demonstrated by Ash and co-workers (34) for electromagnetic waves and Zieniuk et al. (35) for ultrasonic waves. The development of the atomic force microscope has lead to several variants of a near-field acoustic microscope.

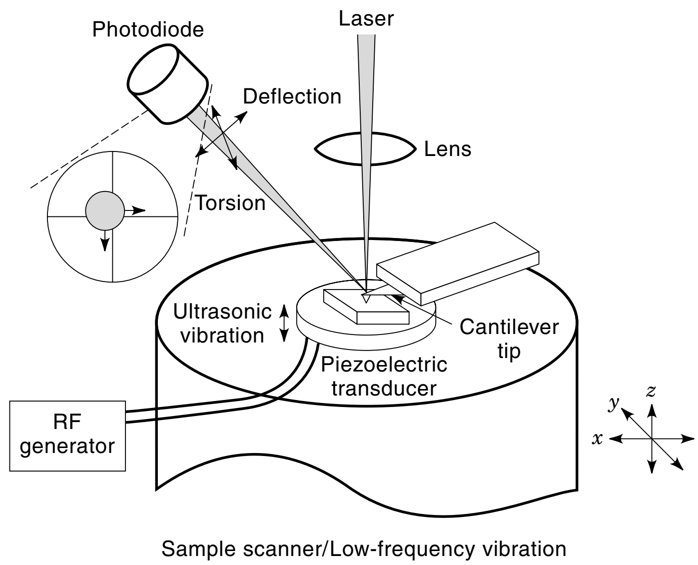

Figure 6. Schematic illustration of an AFM/UFM. A thickness mode PZT transducer is bonded to the sample stage to excite vibrations at 1 MHz to 10 MHz. (From Ref. 38 with permission.)

Takata et al. (36) used a vibrating tip provided by a scanning tunneling microscope, whereby the tip generated strains in the sample, which were detected by a piezoelectric transducer coupled to the sample. The detected signal depended on both the tip-sample interaction and the ultrasonic wave propagation from the tip to the transducer. Cretin et al. (37) have developed microdeformation microscopy, again based on a vibrating tip that is mechanically scanned across the surface, which in this case creates microdeformations in the surface. In transmission mode, a cantilever beam terminated with a diamond or sapphire tip is vibrated at frequencies from 20 kHz to 200 kHz. The microdeformations induce strain in the sample, which is detected by a piezoelectric transducer fixed on to the opposing face. Experiments on silicon wafers and polycrystalline stainless steel showed that the image contrast is related to grain orientation. In the reflection mode, the cantilever is fixed to a piezoelectric transducer; results complementary to transmission are observed.

All of the most recent work is based on the use of the atomic force microscope as the detector of vibrations set up by ultrasonic waves applied to the sample (38). This has the advantage that one can control the frequency, mode direction and amplitude of the applied wave. Most of the work has been done for vertical surface displacements and this will be discussed first. A typical experimental set-up is shown in Fig. 6. The system is integrated with a commercial AFM, and the cantilever displacement is measured optically. Low-frequency scanning for the AFM mode is done in the range 1 kHz to 20 kHz. The sample to be studied is placed on an appropriate piezoelectric transducer. One big advantage of this geometry is that one can very well define the mode, amplitude, and frequency of the driving ultrasonic wave.

In the low-frequency limit, the ultrasonic frequency f is much less than the cantilever resonance frequency f_0; this is called the force modulation mode (FMM). The peak-to-peak cantilever deflection amplitude is given by (38):

$$V = 2z_c \frac{a/z_c}{1 + (k/s)} \tag{23}$$

where a = sample vibration amplitude, k = cantilever spring constant, s = tip-sample contact stiffness, z_c = cantilever deflection due to static repulsive force and $K = k/s$. It is clear that V depends little on K for $K \ll 1$, so we expect little intrinsic contrast for imaging in this regimen. This regimen is also characterized by the absence of tip-sample indentation.

The much more interesting limit, called ultrasonic force microscopy (UFM), corresponds to $f \gg f_0$. At low amplitude, $a < (k/s)z_c$, the average force per cycle on the tip is zero, and so the tip stays on the sample surface. At sufficiently high amplitude a, even though the cantilever cannot follow the ultrasonic vibration, the tip comes away from the sample surface during part of the cycle, as the average tip-sample repulsive force is nonzero. Above the threshold amplitude a_0, the cantilever deflection due to the ultrasound is (38):

$$z_a = z_c\left[\frac{k}{s} + \frac{a}{z_c} + 2\frac{ka}{sz_c} - 2\sqrt{\frac{ka}{sz_c}\left(\frac{k}{s}+1\right)\left(\frac{a}{z_c}+1\right)}\right] \quad a > (k/s)z_c \tag{24}$$

The procedure followed was to amplitude-modulate (triangular) the ultrasonic beam at a frequency below f_0 and measure the cantilever deflection. From Eq. (24), the instrument performance is governed by three factors: (1) normalized cantilever deflection, (2) normalized ultrasonic amplitude a/z and (3) normalized cantilever stiffness $K = k/s$. From Fig. 7 we see that, contrary to the FMM regimen, in the UFM regimen the deflection signal depends strongly on K, so the intrinsic contrast is expected to be high. Thresholds are observed for various values of k/s, and in principle, dynamic elastic effects can be determined from them. The full theory of Hertzian contacts shows that the force curve $F(d)$ is very nonlinear, which is determined in the detection mechanism. The additional cantilever deflection for different repulsive forces and different values of effective elastic constants can be calculated as a function of vibration amplitude; as before, the added deflection is very sensitive to these variations for UFM and not for FMM, leading to the theoretical prediction of good contrast in the former case and not in the latter. Several examples are presented in (38) for UFM vertical mode imaging, principally of defects in HOPG and structure of a floppy disc surface. This work confirms sensitivity of the technique to subsurface elasticity variations and the good image contrast of UFM. Typical fields of view are 400 nm by 500 nm, with ultrasonic frequencies of the order of 5 MHz.

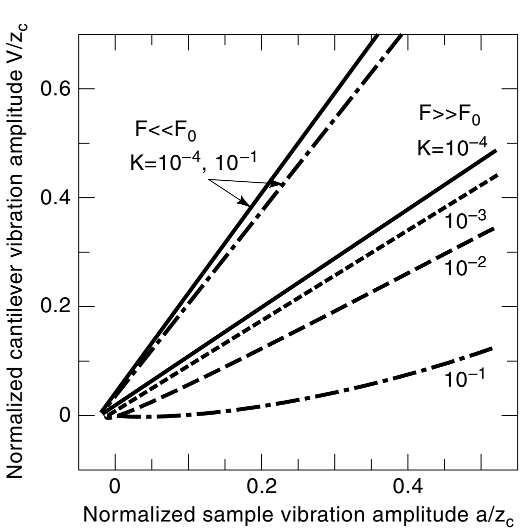

Figure 7. Calculated vibration amplitude in the low frequency FFM mode ($F \ll F_0$) and in the vertical UFM mode ($F \gg F_0$). (From Ref. 39 with permission.)

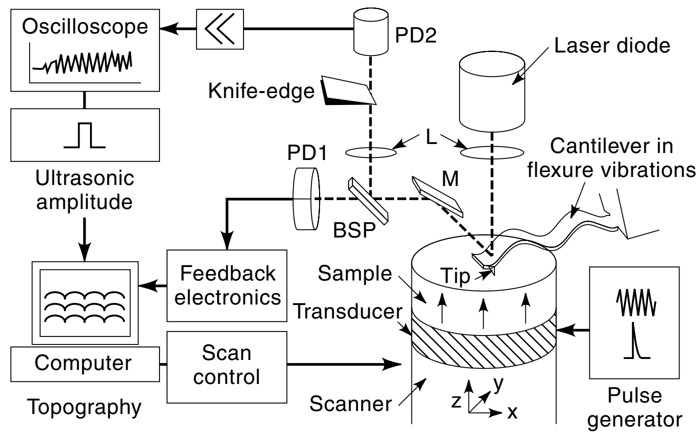

Figure 8. Principle of the AFAM working with high-frequency cantilever vibrations. An ultrasonic transducer is inserted between the scanner and the sample of the AFM. Sample surface vibrations are transmitted into the cantilever and measured with a fast optical knife-edge detector added to the AFM position detector. The signal of the knife-edge detector is amplified and displayed by a digital oscilloscope. For imaging, part of the ultrasonic amplitude is gated out and displayed as an ultrasonic image alongside the topography image. (From Ref. 40 with permission.)

A smaller amount of work has also been done on lateral displacements using the UFM by suitable choice of piezoelectric transducer. For the UFM, the lateral mode AFM (LM-AFM) is based on measurement of the torsional vibration of the cantilever, which is dominated by friction. This principle is used to image the frictional force distribution by amplitude measurement, while the phase gives the energy dissipation. The image is free from topography effects, which are automatically subtracted in real time. There is some indication that the technique is sensitive to subsurface shear modulus variations.

Atomic Force Acoustic Microscopy (AFAM). This is a related study on vertical mode imaging (40), with the experimental arrangement shown in Fig. 8. Again, an ultrasonic transducer in the low MHz range sets up surface vibrations, which are coupled to the tip as described by the mass-spring model. These vibrations excite flexural waves in the cantilever in the MHz range, which can be detected by a very fast knife-edge detector. Resonances of the cantilever surface system can easily be calculated in a mass-spring model and were measured up to mode $n = 9$ by impulse excitation, knife-edge detection, and Fourier transform. The nonlinearity of the tip-sample force is used to explain the ultrasonic coupling to the cantilever. At sufficiently high amplitude, the mean displacement is shifted by nonlinearity, and at very high amplitude, cantilever frequencies other than that used for the ultrasonics are excited. Examples are given of the use of the AFAM for imaging as a function of amplitude; strong variations in contrast are observed, which are interpreted as reflecting the variation in the sound transmission due to the tip-sample interaction forces.

Scanning Local Acceleration Microscopy. The configuration used in this work is again basically similar to that used for the UFM and the AFAM (41), at frequencies much higher than the tip cantilever resonant frequency. Imaging is done in CW at low amplitude in the so-called contact mode. The basic result is that at sufficiently high frequencies the output signal is determined by the cantilever acceleration and not the static force acting on it. The cantilever stays in contact with the sample and the sample stiffness can be mapped as it enters in the interaction stiffness. As before, it has been shown experimentally that the contrast is better than with the AFM, and, moreover, that a contrast variation with frequency predicted by the theory is observed. A "diode" and "subharmonic" mode are identified at higher amplitude, and their interpretation is ongoing.

BIBLIOGRAPHY

1. S. Y. Sokolov, *Dokl. Akad. Nauk,* SSSR **64**: 333, 1949.
2. R. A. Lemons and C. F. Quate, Acoustic microscope—scanning version, *Appl. Phys. Lett.* **24**: 163–165, 1974.
3. R. A. Lemons and C. F. Quate, Acoustic Microscopy, in W. P. Mason and R. N. Thurston (eds.), *Physical Acoustics XIV,* London: Academic, 1979, pp. 1–92.
4. A. Atalar, C. F. Quate, and H. K. Wickramasinghe, Phase imaging in reflection with the acoustic microscope, *Appl. Phys. Lett.* **31** (12): 791–793, 1977.
5. G. A. D. Briggs, *Acoustic Microscopy.* Oxford: The Clarendon Press, 1992.
6. R. D. Weglein and R. G. Wilson, Characteristic material signatures by acoustic microscopy, *Electron. Lett.,* **14** (12): 352–354, 1978.
7. J. Kushibiki and N. Chubachi, Material characterization by line-focus-beam acoustic microscope, *IEEE Trans. Sonics Ultrason.,* **SU-32**: 189–212, 1985.
8. L. W. Kessler, Acoustic microscopy—an industrial view, *IEEE Ultrasonics Symposium,* 725–728, 1988.
9. J. Attal and C. F. Quate, Investigation of some low ultrasonic absorption liquids, *J. Acoust. Soc. Am.,* **59**: 69–73, 1976.
10. J. Heiserman, D. Rugar, and C. F. Quate, Cryogenic acoustic microscopy, *J. Acoust. Soc. Am.,* **67**: 1629–1637, 1980.
11. D. Rugar, Resolution beyond the diffraction limit in the acoustic microscope: a nonlinear effect, *J. Appl. Phys.,* **56**: 1338–1346, 1984.
12. L. Germain and J. D. N. Cheeke, Generation and detection of high-order harmonics in liquids using a scanning acoustic microscope, *J. Acoust. Soc. Amer.,* **83**: 942–949, 1988.
13. C.-H. Chou, B. T. Khuri-Yakub, and G. S. Kino, Lens design for acoustic microscopy, *IEEE Trans. Ultrason. Ferroelectr. Freq. Control,* **UFFC 35**: 464–469, 1988.
14. A. Atalar, An angular spectrum approach to contrast in reflection acoustic microscopy, *J. Appl. Phys.,* **49**: 5130–5139, 1978.
15. R. G. Maev and V. M. Levin, Basic principles of output signal formation in transmission raster acoustic microscopy, *Trans. R. Microsc. Soc.,* **1**: 75–80, 1990.
16. H. L. Bertoni, Ray-optical evaluation of V(z) in the reflection acoustic microscope, *IEEE Trans. Sonics Ultrason.,* **SU-31B**: 105–116, 1984.
17. K. K. Liang, G. S. Kino, and B. Khuri-Yakub, Material characterization by the inversion of V(z), *IEEE Trans. Sonics Ultrason.* **SU-33**: 213–224, 1985.
18. N. N. Hsu et al., Time and polarization resolved ultrasonic measurements using a lenseless line-focus transducer, *IEEE Symposium,* 867–871, 1995.
19. Y. Tsukahara et al., Interaction of acoustic waves with solid surfaces, in A. Briggs and W. Arnold (eds.), *Advances in Acoustic Microscopy Vol. 2,* New York: Plenum Press, 1996, pp. 103–165.
20. F. S. Foster et al., Principles and applications of ultrasound backscatter microscopy, *IEEE Trans. Ultrason. Ferroelectr. Freq. Control,* **UFFC 40**: 608–617, 1993.
21. M. Lethiecq et al., Principles and applications of high-frequency medical imaging, in A. Briggs and W. Arnold (eds.), *Advances in Acoustic Microscopy Vol. 2,* New York: Plenum Press, 1996, pp. 39–98.
22. J. D. Achenbach, J. O. Kim, and Y.-C. Lee, Measuring thin-film constants by line-focus acoustic microscopy, in A. Briggs (ed.), *Advances in Acoustic Microscopy Vol. 1,* New York: Plenum Press, 1995, pp. 153–206.
23. P. Richard, G. Gremaud, and A. Kulik, Thin film adhesion investigations with the acoustic microscope, *IEEE Ultrasonics Symposium,* 1425–1428, 1994.
24. B. T. Khuri-Yakub and P. Rheinholdtsen, Nondestructive evaluation of composite materials using acoustic microscopy, in D. O. Thompson and D. E. Chimenti (eds.), *Review of Progress in Quantitative Nondestructive Evaluation,* **5B**, pp. 1093–1098, 1986.
25. Y.-C. Lee, J. O. Kim, and J. D. Achenbach, Measurement of stresses by line-focus acoustic microscopy, *Ultrasonics,* **32**: 359–365, 1994.
26. K. K. Liang et al., Precise phase measurements with the acoustic microscope, *IEEE Trans. Sonics Ultrason.,* **SU-32**: 266–273, 1985.
27. E. Drescher-Krasicka, Scanning acoustic imaging of stress in the interior of solid materials, *J. Acoust. Soc. Amer.,* **94**: 453–464, 1993.
28. D. Knauss et al., Measuring short cracks by time-resolved acoustic microscopy, in A. Briggs (ed.), *Advances in Acoustic Microscopy Vol. 1,* New York: Plenum Press, 1995, pp. 49–76.
29. R. S. Gilmore et al., Acoustic microscopy from 10 to 100 MHz for industrial applications, *Philos. Trans. R. Soc. London,* **A320**: 215–235, 1986.
30. G. M. Crean, C. M. Flannery, and S. C. O. Mathúna, Acoustic microscopy analysis of microelectronic interconnection and packaging technologies, in A. Briggs (ed.), *Advances in Acoustic Microscopy Vol. 1,* New York: Plenum Press, 1995, pp. 1–45.
31. G. Pfannschmidt, Characterization of electronic components by acoustic microscopy, in A. Briggs and W. Arnold (eds.), *Advances in Acoustic Microscopy Vol. 2,* New York: Plenum Press, pp. 1–38.
32. J. Kushibiki et al., Characterization of 36°YX-$LiTaO_3$ wafers by line-focus-beam acoustic microscopy, *IEEE Trans. Ultrason. Ferroelectr. Freq. Control,* **UFFC 42**: 83–90, 1995.
33. C. K. Jen et al., Characterization of cladded glass fibers using acoustic microscopy, *Appl. Phys.Lett.,* **55**: 2485–2487, 1989.
34. E. A. Ash and N. Nicholls, Super resolution aperture scanning microscope, *Nature,* **237**: 1972.
35. J. K. Zieniuk and L. Latuszek, Non-conventional pin scanning

ultrasonic microscopy, in H. Shimuzu, N. Chubachi, and J. Kushibiki (eds.) *Acoustical Imaging,* New York: Plenum Press, 1989, pp. 219–224.

36. K. Takata et al., Tunneling acoustic microscope, *Appl. Phys. Lett.,* **55**: 1718–1720, 1989.
37. B. Cretin and F. Stahl, Scanning microdeformation microscopy, *Appl. Phys. Lett.,* **62** (8): 829–831, 1993.
38. K. Yamanaka, New approaches in acoustic microscopy for noncontact measurement and ultra high resolution, in A. Briggs (ed.), *Advances in Acoustic Microscopy, Vol. 1,* New York: Plenum Press, 1995, pp. 301–342.
39. K. Yamanaka, H. Ogiso, and O. Kolosov, Ultrasonic force microscopy for nanometer resolution subsurface imaging, *Appl. Phys. Lett.* **64** (2): 178–180, 1994.
40. U. Rabe, K. Janser, and W. Arnold, Acoustic microscopy with resolution in the nm range, in P. Tortolli and L. Masotti (eds.), *Acoustical Imaging,* **22**, New York: Plenum Press, 1996, pp. 669–676.
41. N. A. Burnham et al., Scanning local-acceleration microscopy, *J. Vac. Sci. Technol. B* **14** (2): 794–799, 1996.

DAVID CHEEKE
Concordia University